

# Electronic, optical and transport properties of van der Waals Transition-metal Dichalcogenides Heterostructures: A First-principle Study

Ke Xu<sup>1</sup>, Yuanfeng Xu<sup>1</sup>, Hao Zhang<sup>1†</sup>, Bo Peng<sup>1</sup>, Hezhu Shao<sup>2‡</sup>, Gang Ni<sup>1</sup>, Jing Li<sup>1</sup>, Mingyuan Yao<sup>1</sup>, Hongliang Lu<sup>3</sup>, Heyuan Zhu<sup>1¶</sup> and Costas M. Soukoulis<sup>4,5</sup>

<sup>1</sup>*Department of Optical Science and Engineering,*

*Key Laboratory of Micro and Nano Photonic Structures (MoE) and Key*

*Laboratory for Information Science of Electromagnetic Waves (MoE),*

*Fudan University, Shanghai 200433, China.*

<sup>2</sup>*Ningbo Institute of Materials Technology and Engineering,*

*Chinese Academy of Sciences, Ningbo 315201, China*

<sup>3</sup>*State Key Laboratory of ASIC and System,*

*Institute of Advanced Nanodevices, School of Microelectronics,*

*Fudan University, Shanghai 200433, China*

<sup>4</sup>*Department of Physics and Astronomy and Ames Laboratory,*

*Iowa State University, Ames, Iowa 50011, USA*

<sup>5</sup>*Institute of Electronic Structure and Laser (IESL),*

*FORTH, 71110 Heraklion, Crete, Greece\**

(Dated: January 13, 2022)

Two-dimensional (2D) transition-metal dichalcogenide (TMD)  $\text{MX}_2$  ( $\text{M} = \text{Mo}, \text{W}$ ;  $\text{X} = \text{S}, \text{Se}, \text{Te}$ ) possess unique properties and novel applications. In this work, we perform first-principles calculations on the van der Waals (vdW) stacked  $\text{MX}_2$  heterostructures to investigate their electronic, optical and transport properties systematically. We perform the so-called Anderson's rule to classify the heterostructures by providing the scheme of the construction of energy band diagrams for the heterostructure consisting of two semiconductor materials. For most of the  $\text{MX}_2$  heterostructures, the conduction band maximum (CBM) and valence band minimum (VBM) reside in two separate semiconductors, forming type II band structure, thus the electron-holes pairs are spatially separated. We also find strong interlayer coupling at  $\Gamma$  point after forming  $\text{MX}_2$  heterostructures, even leading to the indirect band gap. While the band structure near  $K$  point remain as the independent monolayer. The carrier mobilities of  $\text{MX}_2$  heterostructures depend on three decisive factors, elastic modulus,

effective mass and deformation potential constant, which are discussed and contrasted with those of monolayer  $\text{MX}_2$ , respectively.

## I. INTRODUCTION

The family of Two-dimensional (2D) materials has grown rapidly for their unique properties different from their 3D counterparts. A wide range of 2D materials, e.g. graphene<sup>1,2</sup>, BN<sup>3,4</sup>, transition metal dichalcogenides (TMDs)<sup>5,6</sup>, black phosphorus<sup>7-9</sup>, and etc, have been proposed and under intense investigations. Among these, transition metal dichalcogenides, with the formula  $\text{MX}_2$  (where M is a transition metal and X is a chalcogen), are prominent due to their finite direct band gaps, with strong optoelectronic responses<sup>10</sup>, large on-off ratios and high carrier mobilities<sup>11,12</sup>. Furthermore, a spin-orbit driven splitting of the valence band was found in the 2H monolayer TMDs due to the lack of inversion symmetry, which ultimately allows for valley-selective excitation of carriers<sup>13-15</sup>. In addition, the electronic properties of TMDs can be tuned by strain<sup>16</sup>, layer numbers<sup>17</sup>, nanostructuring<sup>18</sup>, and electrostatic gating<sup>19</sup>, or by combining individual 2D materials into van der Waals (vdW) stacked heterostructures<sup>20</sup>. The vdW heterostructures can be obtained by transfer or direct epitaxial growth<sup>21,22</sup>. The interface of the heterostructures can be atomically sharp, with two-atomic thick junction region<sup>21</sup>, and the interlayer coupling intensity can even be tuned. Thus, the vdW heterostructures opens up many possibilities for creating new TMD material systems with rich functionalities and novel physical properties<sup>23</sup>. Because when two different atomically thin layers are stacked and binded by van der Waals forces to form  $\text{MX}_2$  heterostructures, electronic properties of the formed vdW  $\text{MX}_2$  heterostructures will be affected significantly by the alignment of the monolayer  $\text{MX}_2$  to form varieties of band structures different from the monolayer counterpart, which can be direct- or indirect-bandgap, or metallic materials<sup>24</sup>.

For example,  $\text{MoS}_2$ - $\text{WSe}_2$  hetero-bilayer possesses a type II band alignment, and furthermore, the conduction band maximum (CBM) and valence band minimum (VBM) reside in different monolayers. Due to the separate spatial locations of CBM and VBM, the photon-generated electron-holes pairs are therefore spatially separated, resulting in much longer exciton lifetime and interlayer exciton condensation, which might help invent two-dimensional lasers, light-emitting diodes and photovoltaic devices.<sup>25,26</sup> And the evidence of strong electronic coupling between the two individual monolayer  $\text{MX}_2$  in  $\text{MoS}_2$ - $\text{WSe}_2$  hetero-bilayer was demonstrated, leading to a new photoluminescence (PL) mode in this heterostructure<sup>27</sup>. Hong *et al* have also investigated the ultrafast charge transfer in  $\text{MoS}_2$ - $\text{WS}_2$  heterostructure<sup>28</sup> and found the charge-transfer time is in femtosecond scale, much smaller than that in monolayer  $\text{MoS}_2$  or  $\text{WS}_2$ . Furthermore, the recombination time of interlayer charge transition is tunable for different stacking order of  $\text{MoS}_2$ -

WS<sub>2</sub> heterostructure (one was obtained by vertical epitaxial growth while the other was randomly bilayer stacked), with 39 ps and 1.5 ns respectively<sup>29</sup>.

To date, most researches on MX<sub>2</sub> heterostructures are concerned about the S and Se system. In this paper, by using first-principles calculations, we systematically investigate the electronic, mechanical, transport and optical properties of the vdW MX<sub>2</sub> (M = Mo, W; X = S, Se, Te) heterostructures. The bandgaps of the hetero-bilayer MX<sub>2</sub> get smaller compared with the corresponding monolayer MX<sub>2</sub>. And the band alignment under Anderson's rule and interlayer coupling of heterostructures can result in direct to indirect bandgap transition. The excellent mechanical properties show the structural stability of the vdW MX<sub>2</sub> heterostructures. The transport properties exhibit encouraging results with the electron mobilities mostly higher than those of the monolayer MX<sub>2</sub>. Furthermore, we also investigate the optical properties of the vdW MX<sub>2</sub> heterostructures.

## II. METHODOLOGY

All the calculations are performed using the Vienna *ab-initio* simulation package (VASP) based on density functional theory (DFT)<sup>30</sup>. The exchange-correlation energy is described by the generalized gradient approximation (GGA) in the Perdew-Burke-Ernzerhof (PBE) parametrization. We choose the DFT-D2 semiempirical dispersion-correction approach to involve the long-distance van der Waals (vdW) interactions<sup>31,32</sup>. The calculation is carried out by using the projector-augmented-wave (PAW) pseudopotential method with a plane-wave basis set with a kinetic energy cutoff of 600 eV. A 15×15×1  $\Gamma$ -centered **k**-mesh is used during structural relaxation for the unit cell until the energy differences are converged within 10<sup>-6</sup> eV, with a Hellman-Feynman force convergence threshold of 10<sup>-4</sup> eV/Å. The vacuum size is larger than 25 Å between two adjacent atomic layers to eliminate artificial interactions between them. The electronic bandstructures of the vdW layered heterostructures are further verified by the calculations using hybrid Heyd-Scuseria-Ernzerhof (HSE06) functional<sup>33,34</sup>, which improves the precision of bandstructures by reducing the localization and delocalization errors of PBE and Hartree-Fock (HF) functionals. Here the mixing ratio is 25% for the short-range HF exchange. The screening parameter is 0.2 Å<sup>-1</sup>.

As we know, the electron-phonon scatterings play an important role in determining the intrinsic carrier mobility  $\mu$  of 2D vdW MX<sub>2</sub> heterostructures, in which the scattering intensities by acoustic phonons are much stronger than those by optic phonons in two-dimensional materials<sup>35</sup>. Therefore, the deformation potential theory for semiconductors, which considers only longitudinal

acoustic phonon scattering process in the long-wavelength limit<sup>36–39</sup>, and was originally proposed by Bardeen and Shockley<sup>40</sup>, can be used to calculate the intrinsic carrier mobility of 2D materials. In the long-wavelength limit, the carrier mobility of 2D semiconductors can be written as<sup>39,41,42</sup>:

$$\mu = \frac{2e\hbar^3 C}{3k_B T |m^*|^2 D_l^2}, \quad (1)$$

where  $e$  is the electron charge,  $\hbar$  is the reduced Planck's constant,  $T$  is the temperature equal to 300 K throughout the paper.  $C$  is the elastic modulus of a uniformly deformed crystal by strains and derived from  $C = [\partial^2 E / \partial^2 (\Delta l / l_0)] / S_0$ , in which  $E$  is the total energy,  $\Delta l$  represents the change of lattice constant  $l_0$  along the strain direction, and  $S_0$  is the lattice area at equilibrium for a 2D system.  $m^*$  is the effective mass given by  $m^* = \hbar^2 (\partial^2 E(k) / \partial k^2)^{-1}$  ( $k$  is wave-vector, and  $E(k)$  is the energy). In addition,  $D_l$  is the deformation potential (DP) constant defined by  $D_l^{e(h)} = \Delta E_{CBM(VBM)} / (\Delta l / l_0)$ , where  $\Delta E_{CBM(VBM)}$  is the energy shift of the band edge with respect to the vacuum level under a small dilation  $\Delta l$  of the lattice constant  $l_0$ .

### III. RESULTS AND DISCUSSION

#### A. Geometric structures of hetero-bilayer $\text{MX}_2$

Generally, the  $\text{MX}_2$  crystals have four stable lattice structures, i.e., 2H, 1T, 1T' and 3R<sup>43</sup>, with the first being the dominating one in nature. Most  $\text{MX}_2$  crystals, like  $\text{MoS}_2$  and  $\text{WSe}_2$  with a stable 2H phase (1H for monolayer), have been studied widely<sup>44</sup>. For 2H-phase  $\text{MX}_2$  crystals, the M atoms and X atoms are located in different layers respectively, which can be described by the point group  $D_{3h}$ . While for the 3R-phase unit cell shown as Fig. 1(b,d), one M atom is eclipsed by the X atoms above and the other one is located in the hexagonal center, leading to the AB Bernal stacking. Here, we only focused on the AA and AB Bernal stacking. One stacking type can be transformed to the other one by horizontal sliding or by the rotation around the vertical axis. For  $\text{MX}_2$  heterostructures with two different constituent monolayer  $\text{MX}_2$  crystals, both AA and AB Bernal stacking possess a lower symmetry of  $C_{3v}$  point group due to the lack of the mirror reflection  $\sigma_h$  in the horizontal plane. The symmetry operations include  $C_3$  and vertical mirror reflection  $\sigma_v$ <sup>45</sup>. When the two constituent monolayer  $\text{MX}_2$  crystals are identical, the AA stacking still possesses  $D_{3h}$  symmetry.

To determine the energetically stable structure before geometry optimization, an interlayer-

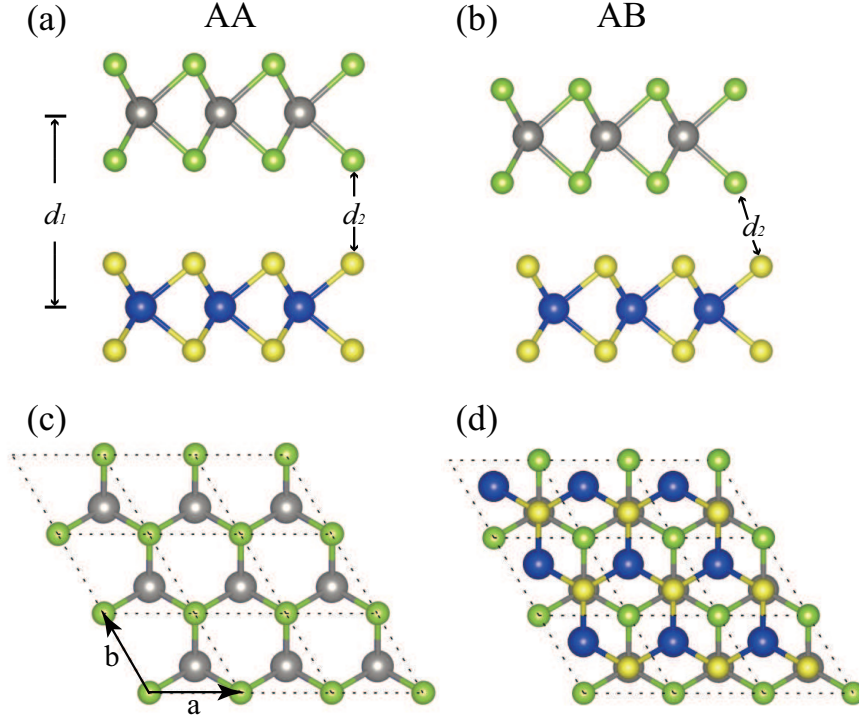


FIG. 1. Atomic structure of AA stacking and AB stacking hetero-bilayer  $MX_2$  in a  $3 \times 3 \times 1$  supercell from side view (upper panel) and top view (lower panel), respectively. Large and small spheres represent the M and X atoms, respectively. A color coding is used to distinguish the different atomic species.  $d_1$  and  $d_2$  are the interlayer distance ( $M_1-M_2$ ) and the bond length of  $X_1-X_2$ .

distance optimization step is implemented to find out an optimized  $d$  (defined in the Fig. 1(a)) using the so-called Universal Binding Energy Relation (UBER) method<sup>46,47</sup>. The optimized interlayer distance is predicted from a series of unrelaxed models with different  $d$  (from 5 to 8 Å), and then we calculate the surface adhesion energy  $W_{ad}$  for all 30 types of 2D vdW  $MX_2$  heterostructures under investigations here (take  $MoS_2/WSe_2$  hetero-bilayer as an example),

$$W_{ad} = \frac{E_{MoS_2} + E_{WSe_2} - E_{MoS_2/WSe_2}}{A}, \quad (2)$$

where  $A$  is the interface area and  $E_{MoS_2}$ ,  $E_{WSe_2}$ ,  $E_{MoS_2/WSe_2}$  are the total energies of the monolayer  $MoS_2$ ,  $WSe_2$  and the  $MoS_2/WSe_2$  heterostructure, respectively. The optimal interlayer distances  $d$  can be obtained by maximizing the value of  $W_{ad}$ . Then the obtained optimized structure was further optimized again without any external constraints.

The calculated lattice constant  $a$  and interlayer distance  $d$  for the above-mentioned 30 types of 2D  $MX_2$  heterostructures are summarized in the TABLE I, which are in good consistence with

TABLE I. Hetero-bilayer system and band alignment type, optimized lattice constant  $a$  (Å), interlayer distance  $d_1$  (Å) and the atomic distance  $d_2$  (Å) between the adjacent anion in different layers, band gap of MX<sub>2</sub> heterostructure (PBE/HSE/SOC). Other theoretical data are also listed in parentheses for comparison

System (Anderson)	Stacking type	$a$ (Å)	$d_1$ (Å)	$d_2$ (Å)	Band type	$E_g^{PBE} / E_g^{HSE} / E_g^{SOC}$ (eV)
MoS <sub>2</sub> -WSe <sub>2</sub> (II)	AA	3.251 (3.26 <sup>51</sup> )	6.919	4.896	Direct	0.46(0.57 <sup>51</sup> )/1.01/0.23
	AB	3.256	6.270	3.580	Direct	0.57/1.12/0.34
MoS <sub>2</sub> -WS <sub>2</sub> (II)	AA	3.183 (3.19 <sup>51</sup> )	6.758 (6.8 <sup>52</sup> )	4.826	Indirect	1.29(1.16 <sup>51</sup> )/1.93/1.22
	AB	3.187	6.137 (6.3 <sup>52</sup> )	3.535	Indirect	1.08/1.70/1.06
WS <sub>2</sub> -WSe <sub>2</sub> (II)	AA	3.250 (3.204 <sup>24</sup> )	6.852	4.846	Direct	0.77(1.007 <sup>24</sup> )/1.24/0.51
	AB	3.253	6.232	3.547	Indirect	0.80/1.31/0.61
MoSe <sub>2</sub> -WS <sub>2</sub> (II)	AA	3.249 (3.210 <sup>24</sup> )	6.913	4.893	Direct	1.23 (1.154 <sup>24</sup> )/1.34/0.85
	AB	3.251	6.303	3.613	Indirect	0.86/1.27/0.80
MoSe <sub>2</sub> -WSe <sub>2</sub> (II)	AA	3.320 (3.277 <sup>24</sup> )	7.078	3.745	Direct	1.23 (1.330 <sup>24</sup> )/1.79/0.93
	AB	3.307	6.485	3.680	Indirect	1.21/1.83/1.09
MoS <sub>2</sub> -MoSe <sub>2</sub> (II)	AA	3.250 (3.26 <sup>51</sup> )	6.972	4.940	Direct	0.98(0.74 <sup>51</sup> )/1.10/0.56
	AB	3.254	6.350	3.655	Direct	0.65/1.09/0.56
MoTe <sub>2</sub> -MoS <sub>2</sub> (II)	AA	3.328	7.267	5.058	–	–/0.45/–
	AB	3.347	6.575	3.736	–	–/0.47/–
MoTe <sub>2</sub> -MoSe <sub>2</sub> (II)	AA	3.413	7.421	5.177	Indirect	0.49/0.95/0.19
	AB	3.413	6.784	3.853	Indirect	0.51/0.95/0.21
MoTe <sub>2</sub> -WS <sub>2</sub> (II)	AA	3.347	7.170	4.984	–	–/0.43/–
	AB	3.350	6.576	3.757	–	–/0.42/–
MoTe <sub>2</sub> -WSe <sub>2</sub> (I)	AA	3.425	7.354	5.136	Indirect	0.69/1.05/0.60
	AB	3.423	6.725	3.811	Indirect	0.64/1.00/0.53
MoTe <sub>2</sub> -WTe <sub>2</sub> (II)	AA	3.538	7.646	5.348	Direct	0.95/1.44/0.67
	AB	3.543	6.954	3.923	Indirect	0.93/1.46/0.74
WTe <sub>2</sub> -MoS <sub>2</sub> (III)	AA	3.354	7.204	5.018	–	–/0.46/–
	AB	3.358	6.584	3.751	–	–/0.37/–
WTe <sub>2</sub> -MoSe <sub>2</sub> (II)	AA	3.423	7.358	5.128	Direct	0.33/0.85/0.10
	AB	3.429	6.740	3.833	Direct	0.35/0.84/0.11
WTe <sub>2</sub> -WS <sub>2</sub> (III)	AA	3.360	7.114	4.963	–	–/0.41/–
	AB	3.365	6.516	3.717	–	–/0.40/–
WTe <sub>2</sub> -WSe <sub>2</sub> (I)	AA	3.422	7.288	5.092	Direct	0.51/0.93/0.24
	AB	3.447	6.679	3.781	Direct	0.45/0.86/0.17

previous theoretical and experimental results of the monolayer MX<sub>2</sub><sup>48–50</sup>. and are not sensitive to the interlayer distance. As shown in TABLE I, the optimized interlayer distances of AA stacking structures are larger than those of the corresponding AB stacking structures, which is due to the fact that, in AB structures, the X atoms are not aligned along the vertical axis and a shorter interlayer distance leads to a smaller total energy. Since the M atoms in different layers almost has no interactions, the change of stacking type will affect the interlayer interactions of X atoms.

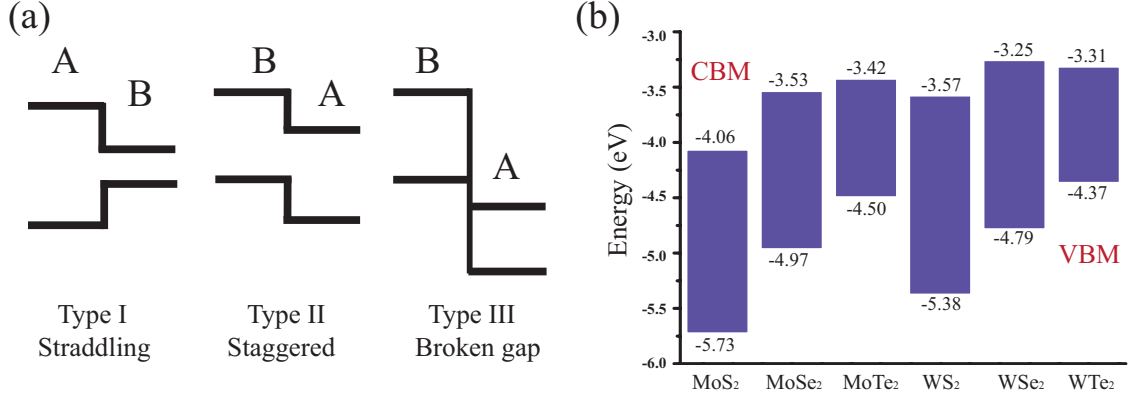


FIG. 2. (a) Various possible bandedge lineups in semiconductor A and B. (b) Band alignment for monolayer  $\text{MX}_2$ . The vacuum level is taken as 0 reference.

### B. Electronic band structure of hetero-bilayer $\text{MX}_2$

Previous studies on TMDs have revealed that the monolayer  $\text{MX}_2$  possesses direct band gap, and the conduction band maximum (CBM) and valence band minimum (VBM) located at K point<sup>17,53–55</sup>. Owing to the lack of inversion symmetry and the strong SOC effect, the valence bands possess a significant spin-orbit splitting at K valleys<sup>56</sup>. And the band alignment for  $\text{MX}_2$  shows the following trends (see from Fig. 2(b)) For common-X system, the band gap of  $\text{MoX}_2$  are larger than that of  $\text{WX}_2$ , and the CBM and VBM of  $\text{WX}_2$  are higher than those of  $\text{MoX}_2$ ; 2) For common-M system, an increase of the atomic number of X results in a shallower anion  $p$  orbital and thus a shift of the VBM to higher energies, finally leading to decreased band gaps<sup>57</sup>. To understand these two trends in band alignment, the atomic orbital composition of the states should be taken into consideration. Taking  $\text{MoS}_2$  as an example, the CBM of  $\text{MoS}_2$  is mainly composed by the  $d_{z^2}$  orbital of Mo and the  $p_x$  and  $p_y$  orbitals of S, whereas the VBM mostly consists of the  $d_{x^2-y^2}$  and  $d_{xy}$  orbitals of Mo.

For the hetero-bilayer  $\text{MX}_2$  crystals constructed by two monolayer  $\text{MX}_2$ , their band structures can be understood by the so-called Anderson's rule, which provides the scheme of the construction of energy band diagrams for the heterostructure consisting of two semiconductor materials<sup>58</sup>. According to the Anderson's rule, the vacuum energy levels of the two constituent semiconductors on either side of the heterostructure should be aligned at the same energy<sup>59</sup>, and there are three types of possible bandedge lineups: straddling, staggered and broken gap, as shown in Fig. 2(a). For type I heterostructure, the conduction band maximum (CBM) and valence band minimum (VBM)



mainly consist of the orbitals of semiconductor B, which possesses a smaller band gap compared to semiconductor A. Thus, the band type of the heterostructure is consistent with the smaller-gap material. For type II heterostructure, the VBM and the CBM around the Fermi level reside in two separate semiconductors, and the formed heterostructure still possesses a small direct or indirect band gap. As for type III heterostructure, the locations of CBM and VBM are similar to those of type II heterostructure, but there does not exist band gap, and the formed heterostructure is a semimetal. It should be noted that, for type II and type III heterostructures, since the CBM and VBM may locate on different semiconductors, the photon-generated excitons are thus spatially separated, which will suppress the recombination of electron-hole pairs and extend the excitons lifetimes compared with the corresponding individual semiconductors<sup>25,26,54,60–62</sup>.

The band types and bandgaps for the vdW  $\text{MX}_2$  heterostructures are calculated by the PBE and HSE06 method and the results are shown in TABLE I. The direct band gap at K point for monolayer  $\text{MX}_2$  is transformed into three types of band gaps when a hetero-bilayer  $\text{MX}_2$  crystal is formed, i.e., direct, indirect ( $\Gamma$ -K, M-K) and zero bandgap or overlapping bands, according to the calculated results shown in TABLE I and the above-mentioned analysis based on the Anderson's rule. The formation type of the band gap for the vdW  $\text{MX}_2$  heterostructures categorized according to the Anderson's rule is also shown in TABLE I. The classification of the band types according to the Anderson's rule is called as Anderson band type hereafter. It is shown in TABLE I that, the Anderson band types for the vdW  $\text{MX}_2$  are determined by the constituent monolayer  $\text{MX}_2$  irrespective of the stacking manner, which is probably due to the fact the VBM/CBM of hetero-bilayer structure is attributed to the  $d/p$ -orbitals of M/X atoms, and the weak vdW interactions will not change the charge distribution of the substituent monolayer  $\text{MX}_2$  of the hetero-bilayer structure significantly.

For simplicity, we first consider the Anderson band type I heterostructure, e.g. band structures for  $\text{WTe}_2$ - $\text{WSe}_2$  and  $\text{MoTe}_2$ - $\text{WSe}_2$  hetero-bilayer structures shown as Fig. 3(a,b). Generally, as we mentioned above, two monolayer  $\text{MX}_2$  crystals with identical M atoms but different X atoms possess different CBM/VBM energy levels, and the crystal with the X atoms with a larger atomic number has a higher energy level of CBM or VBM. However, as shown in Fig. 2(b), the CBM energy-level of  $\text{WTe}_2$  is lower than that of  $\text{WSe}_2$ , although the atomic number of Te is larger than Se. Such a deviation can be understood by the fact that the bond length  $d_{\text{W-Te}}$  of  $\text{WTe}_2$  is the largest one among the monolayer  $\text{MX}_2$  crystals, which leads to a small overlap integral  $V$  between  $d$  orbitals of M atoms and  $p$  orbitals of X atoms for the formation of CBM due to

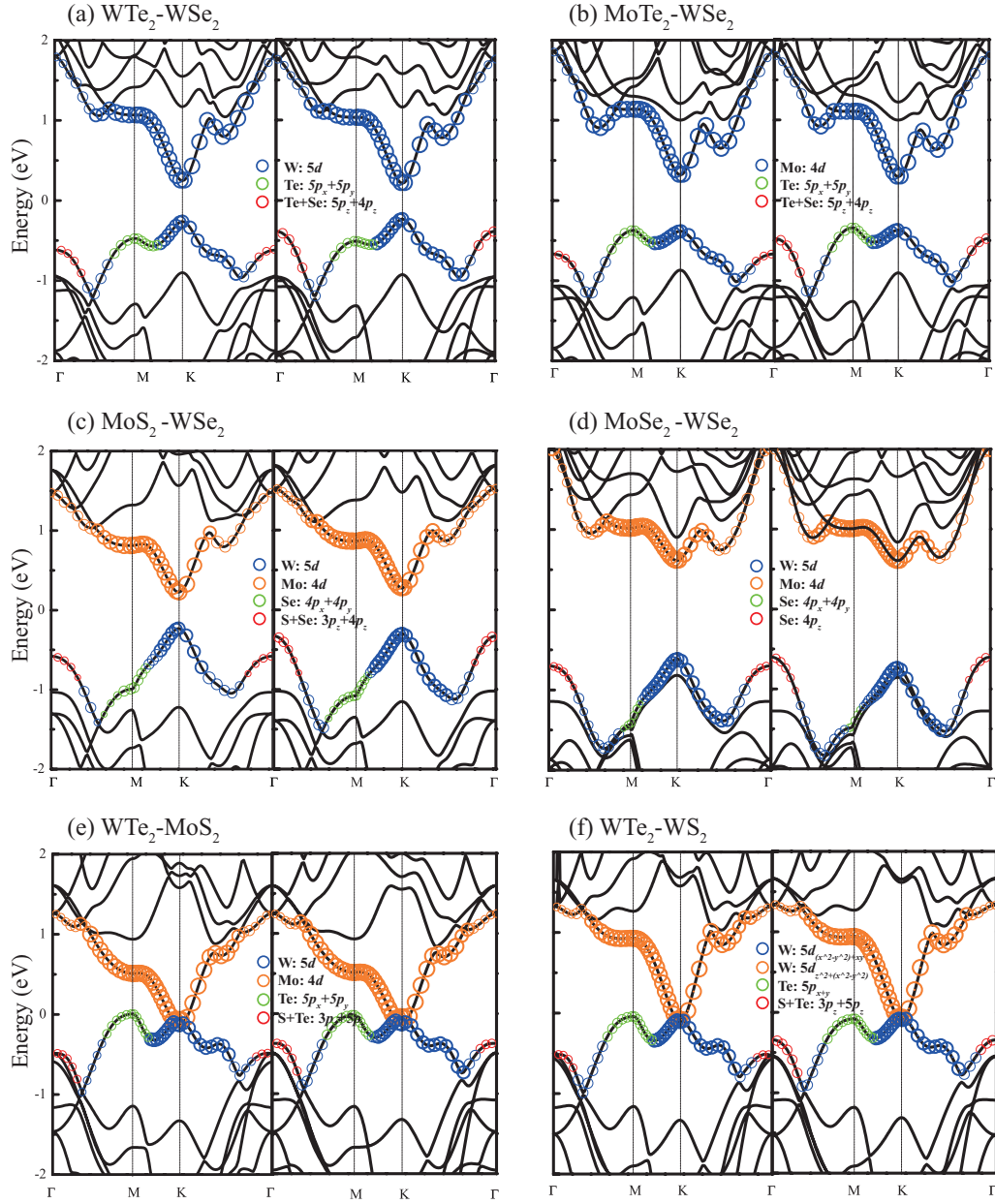


FIG. 3. Band structures of the AA and AB stacking vdW MX<sub>2</sub> heterostructures and atomic orbital weights in the energy bands. The blue and orange circles represent *d* orbitals of the cations. The green and red circles represent *p<sub>x</sub> + p<sub>y</sub>* and *p<sub>z</sub>* orbitals of the anions, respectively. The size of each circle is proportional to the weight of the atomic orbital. (a)(b) Type I band alignment system: WTe<sub>2</sub>-WSe<sub>2</sub> and MoTe<sub>2</sub>-WSe<sub>2</sub> hetero-bilayer. (c)(d) Type II band alignment system: MoS<sub>2</sub>-WSe<sub>2</sub> and MoSe<sub>2</sub>-WSe<sub>2</sub> hetero-bilayer. (e)(f) Type III band alignment system: WTe<sub>2</sub>-MoS<sub>2</sub> and WTe<sub>2</sub>-WS<sub>2</sub> hetero-bilayer.

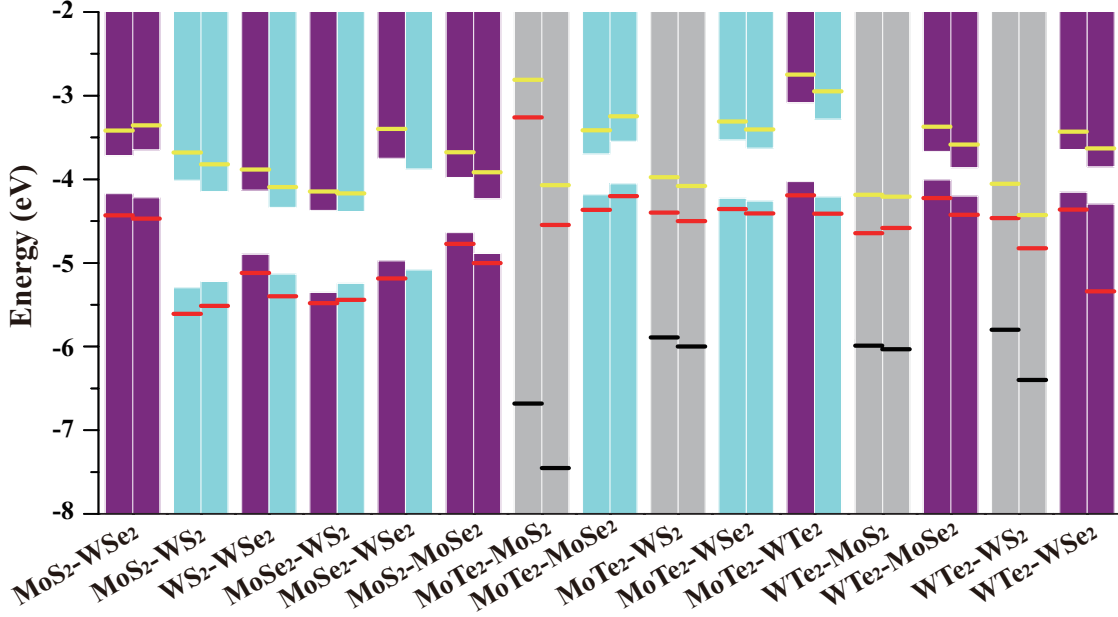


FIG. 4. Calculated band alignment for the vdW MX<sub>2</sub> heterostructures. The histogram is obtained by PBE, with the purple, blue and grey representing the direct bandgap, indirect bandgap and zero-bandgap, respectively. The red and yellow solid lines represent the VBM and the CBM obtained by HSE.

$V \propto 1/d_{W-Te}^2$ <sup>63,64</sup>, and thus counteracts the increase of CBM energy level from Se with a swallower  $p$  orbitals compared to Te<sup>54</sup>. The smaller CBM energy-level of WTe<sub>2</sub> ultimately results in the Anderson band type-I alignment of band edges in WTe<sub>2</sub>-WSe<sub>2</sub> hetero-bilayer, which possesses a direct bandgap at  $K$  point for both AA and AB stacking manners, as shown in Fig. 3(a).

As shown in Fig. 3, the valence band at the  $M$  point is attributed to the  $p_x$  and  $p_y$  orbitals of X atoms, and the corresponding energy level for hetero-bilayer MX<sub>2</sub> crystals containing Te atoms is larger than those containing Se or S atoms, since the mass of Te is the largest one. Therefore, for hetero-bilayer MTe<sub>2</sub>-MX<sub>2</sub>, the valence band energies at  $M$  point significantly increase compared with the hetero-bilayer MSe<sub>2</sub>-MX<sub>2</sub> ( $X \neq Te$ ) or MS<sub>2</sub>-MX<sub>2</sub> ( $X \neq Te$ ), which subsequently leads to the formation of the  $M - K$  indirect band gap for the Anderson band type I heterostructure, e.g. hetero-bilayer MoTe<sub>2</sub>-WSe<sub>2</sub>, as shown in Fig. 3(b).

As shown in TABLE I, most of the hetero-bilayer MX<sub>2</sub> crystals are the Anderson band type II heterostructure, e.g., hetero-bilayer MoS<sub>2</sub>-WSe<sub>2</sub> and MoSe<sub>2</sub>-WSe<sub>2</sub>. Fig. 3(c,d) show the energy band structures of the AA and AB stacking MoS<sub>2</sub>-WSe<sub>2</sub> hetero-bilayers, exhibiting direct bandgaps of 0.46eV and 0.57eV for AA and AB stacking type, respectively, which are consistent with the previous results<sup>65</sup>. The CBM locates on the MoS<sub>2</sub> layer and the VBM locates on the

WSe<sub>2</sub> layer, resulting in the formation of spatially separated electron-hole pairs. Experiments on hetero-bilayer MoS<sub>2</sub>-WSe<sub>2</sub> revealed the dramatically quenching of the photoluminescence (PL) intensities<sup>27</sup>, and the extended exciton lifetime<sup>26</sup>.

The valence band at the  $\Gamma$  point can be attributed to the inter-layer overlap integral of  $p_z$  orbitals of X atoms belonging to different monolayers at  $\Gamma$  point, as shown in Fig. 3. For hetero-bilayer MX<sub>2</sub> considered here, the distance between X atoms belonging to different monolayers for the AB stacking hetero-bilayer, i.e.  $d_2$  shown in Fig. 1(a,b), is smaller than the corresponding AA stacking hetero-bilayer, as shown in TABLE I, thus the energy level of the valence band at the  $\Gamma$  point for AB stacking hetero-bilayer is larger than that for AA stacking hetero-bilayer, due to  $V_{p_z-p_z} \propto 1/d_2^2$ . The increase of the energy level of the valence band at  $\Gamma$  points sometimes leads to the formation of  $\Gamma - K$  indirect band gap, e.g. MoSe<sub>2</sub>-WSe<sub>2</sub> as shown in Fig. 3(d).

The extreme state of staggering is the formation of broken bandgaps, which is also called as the Anderson band type III alignment, as shown in Fig. 2(a). For example, the CBMs of MoS<sub>2</sub> and WS<sub>2</sub> are much lower than that of other monolayer MX<sub>2</sub> and the WTe<sub>2</sub> possess the highest VBM, as shown in Fig. 2(b), the band alignment in hetero-bilayer WTe<sub>2</sub>-MoS<sub>2</sub> and WTe<sub>2</sub>-WS<sub>2</sub> thus can be approximately considered as the Anderson band type III alignment, as shown in Fig. 3(e,f). The band overlaps at  $K$  point, changing the heterostructures into metallic phase.

The bandgaps of the hetero-bilayer MX<sub>2</sub> crystals based on the HSE and SOC calculations are also provided in TABLE I. The negative SOC effects decrease the band gap and the HSE calculations increase the band gap by 0.4-0.6 eV, compared to the bandgap values calculated by PBE calculations. It should be noted that the metallic phases of the hetero-bilayer MX<sub>2</sub> crystals, i.e. the Anderson band type III heterostructures, e.g. hetero-bilayer WTe<sub>2</sub>-MoS<sub>2</sub> and WTe<sub>2</sub>-WS<sub>2</sub> crystals as shown in Fig. 3(e,f), are replaced by direct bandgap phases based on the more precise HSE calculations, which means that the hetero-bilayer MX<sub>2</sub> crystals considered here does not possess the Anderson band type III alignment.

### C. Mechanical properties and transport properties of hetero-bilayer MX<sub>2</sub>

Since the MX<sub>2</sub> heterostructures under considerations here possess  $C_{3v}$  symmetry, which means that the number of independent second-order elastic coefficients  $c_{ij}$  is five and  $c_{11} = c_{22}$ <sup>66</sup>. The calculated elastic coefficients of all MX<sub>2</sub> heterostructures are shown in TABLE S2, and all the

TABLE II. Hetero-bilayer system and band alignment type, Young's modulus  $Y(GPa)$  and Poisson's ratio  $\nu$ , electron and hole effective masses along armchair direction, deformation potential constants for CBM and VBM, elastic modulus, electron and hole mobilities along armchair direction.

System (Anderson)	Stacking type	$Y(N/m)$	$\nu$	$m_e^*(m_0)$	$m_h^*(m_0)$	$D_l^e$	$D_l^h$	$C$ ( N/m )	$\mu_e(\text{cm}^2/(\text{V}\cdot\text{s}))$	$\mu_h(\text{cm}^2/(\text{V}\cdot\text{s}))$
MoS <sub>2</sub> -WSe <sub>2</sub> (II)	AA	209.95	0.29	0.47	0.46	3.03	2.88	118.58	896.07	873.17
	AB	225.30	0.23	0.47	0.46	2.96	3.52	111.47	565.41	873.1
MoS <sub>2</sub> -WS <sub>2</sub> (II)	AA	241.46	0.25	0.46	1.70	6.01	5.70	127.81	256.46	18.04
	AB	242.03	0.24	0.46	0.92	6.28	5.03	121.19	318.08	76.7
WS <sub>2</sub> -WSe <sub>2</sub> (II)	AA	206.89	0.25	0.28	0.46	3.33	3.27	114.74	1939.55	709.71
	AB	218.60	0.20	0.28	0.85	5.65	4.88	118.01	895.83	75.47
MoSe <sub>2</sub> -WS <sub>2</sub> (II)	AA	272.60	0.31	0.28	0.71	3.10	3.25	119.6	2005.27	360.99
	AB	263.53	0.30	0.28	0.97	5.28	4.61	112.98	940.06	63.53
MoSe <sub>2</sub> -WSe <sub>2</sub> (II)	AA	206.94	0.25	0.54	0.44	2.14	2.66	109.98	758.95	1871.24
	AB	215.79	0.22	0.56	1.29	4.01	3.24	111.32	477.54	61.56
MoS <sub>2</sub> -MoSe <sub>2</sub> (II)	AA	232.78	0.26	0.42	0.71	2.87	2.78	125.83	1321.55	454.69
	AB	230.26	0.27	0.42	0.71	3.07	4.50	114.86	758.03	359.04
MoTe <sub>2</sub> -MoS <sub>2</sub> (II)	AA	196.82	0.36							
	AB	196.87	0.34							
MoTe <sub>2</sub> -MoSe <sub>2</sub> (II)	AA	184.77	0.31	0.46	1.37	4.40	3.74	113.18	532.75	45.79
	AB	200.46	0.25	0.46	1.37	4.07	3.75	110.81	532.75	45.79
MoTe <sub>2</sub> -WS <sub>2</sub> (II)	AA	206.17	0.28							
	AB	195.86	0.31							
MoTe <sub>2</sub> -WSe <sub>2</sub> (I)	AA	183.70	0.28	0.30	1.33	3.95	3.83	109.1	515.87	52.52
	AB	194.71	0.24	0.30	1.25	4.41	4.14	114.79	1191.02	58.76
MoTe <sub>2</sub> -WTe <sub>2</sub> (II)	AA	136.33	0.39	0.57	0.42	1.61	1.38	101.62	1023.61	55.76
	AB	171.83	0.22	0.58	3.46	4.32	3.30	99.43	2315.94	3285.72
WTe <sub>2</sub> -MoS <sub>2</sub> (III)	AA	169.33	0.20							
	AB	189.09	0.28							
WTe <sub>2</sub> -MoSe <sub>2</sub> (II)	AA	183.83	0.27	0.45	0.48	2.65	2.85	109.47	382.87	6.58
	AB	196.41	0.22	0.45	0.48	2.70	2.85	102.26	912.5	987.31
WTe <sub>2</sub> -WS <sub>2</sub> (III)	AA	189.00	0.20							
	AB	233.27	0.29							
WTe <sub>2</sub> -WSe <sub>2</sub> (I)	AA	168.36	0.33	0.30	0.46	2.95	2.97	113.4	912.5	987.31
	AB	197.77	0.22	0.30	0.45	2.79	3.08	115.65	875.3	918.66

vdW MX<sub>2</sub> heterostructures are mechanically stable, according to the Born criteria<sup>67</sup>,

$$C_{11} - C_{12} > 0, C_{11} + 2C_{12} > 0, C_{44} > 0 \quad (3)$$

The 2D Young's modulus of all MX<sub>2</sub> heterostructures, given by  $Y^{2D} = \frac{c_{11}c_{22}-c_{12}^2}{c_{11}}$ <sup>68</sup>, are listed in TABLE II. The 2D Young's modulus for monolayer MX<sub>2</sub> crystals decrease from MS<sub>2</sub> to MSe<sub>2</sub> to MTe<sub>2</sub><sup>69</sup>, which is due to the fact that, the strength of  $d_{xy,yz,zx} - p$ -orbital coupling, which forms M-X bonding, becomes weaker with an increase of the atomic number of chalcogen<sup>70</sup>. The calculated

2D Young's modulus for monolayer  $\text{MX}_2$  crystals are shown in TABLE S1. The contributions to the mechanical properties of  $\text{MX}_2$  heterostructures can be roughly considered from constituent monolayer  $\text{MX}_2$  crystals and the interlayer bonding.

The Young's modulus of the  $\text{MTe}_2$ - $\text{MX}_2$  heterostructures are lower than others due to the weakest  $Y^{2D}$  of monolayer  $\text{MTe}_2$  among the monolayer  $\text{MX}_2$  crystals considered here. Meanwhile, the Young's modulus of the  $\text{MX}_2$  heterostructures are a little lower than the sum of those of the corresponding monolayer  $\text{MX}_2$  crystals, which means that the contribution from the interlayer bonding to the total Young's modulus is negative. The Poisson's ratios given by  $\nu^{2D} = \frac{c_{12}}{c_{22}}$ <sup>68</sup>, which describes the lateral deformation when applying uniaxial strains, are calculated and shown in TABLE II. Generally materials with high Poisson's ratio possess good plasticity. The Poisson's ratios for the  $\text{MX}_2$  heterostructures are numerically close to each other except  $\text{WTe}_2$ - $\text{MX}_2$ , due to the lowest Poisson's ratio of 0.20 of monolayer  $\text{WTe}_2$  crystal among the monolayer  $\text{MX}_2$  crystals (see TABLE S1).

The calculated effective masses for electrons  $m_e^*$  and holes  $m_h^*$  of vdW  $\text{MX}_2$  heterostructures are shown in TABLE I. The values of  $m_e^*$  for AA-stacking  $\text{MX}_2$  heterostructures are close to those of the corresponding AB-stacking ones, however, the values of  $m_h^*$  for AA-stacking heterostructures are deviated obviously from those of AB-stacking ones, e.g.  $\text{MoS}_2$ - $\text{WS}_2$  and  $\text{MoTe}_2$ - $\text{WTe}_2$  heterostructures, especially when the band types for AA and AB stackings are different (direct vs indirect), as shown in TABLE I and II. Such phenomena can be understood by the stable location of CBM (electrons) at  $K$  point for all the  $\text{MX}_2$  heterostructures, and the transition of VBM (holes) from  $K$  point to  $M$  or  $\Gamma$  point for  $\text{MX}_2$  heterostructures with an indirect band gap.

As mentioned above, the bandstructures of  $\text{MX}_2$  heterostructures can be roughly decomposed into those of the constituent monolayer  $\text{MX}_2$  crystals, according to the Anderson's rule, which also leads to the formation of the effective masses of electrons and holes for  $\text{MX}_2$  heterostructures. Fig. 5 shows the effective masses of electrons and holes for  $\text{MX}_2$  heterostructures and the corresponding constituent monolayer  $\text{MX}_2$  crystals along all directions, taking  $\text{WTe}_2$ - $\text{WSe}_2$  and  $\text{MoS}_2$ - $\text{WSe}_2$  hetero-bilayer as examples without loss of generality.

The  $\text{WTe}_2$ - $\text{WSe}_2$  hetero-bilayer belongs to the Anderson band type I and the CBM and VBM are attributed to those of monolayer  $\text{WTe}_2$  crystal. It is shown in Fig. 5(a,b) that the effective masses of electrons and holes for the  $\text{WTe}_2$ - $\text{WSe}_2$  hetero-bilayer are close to those of monolayer  $\text{WTe}_2$  crystals, respectively. However, for  $\text{MoS}_2$ - $\text{WSe}_2$  hetero-bilayer (Anderson band type II), since the CBM is attributed to that of monolayer  $\text{MoS}_2$  crystal and VBM is attributed to that of



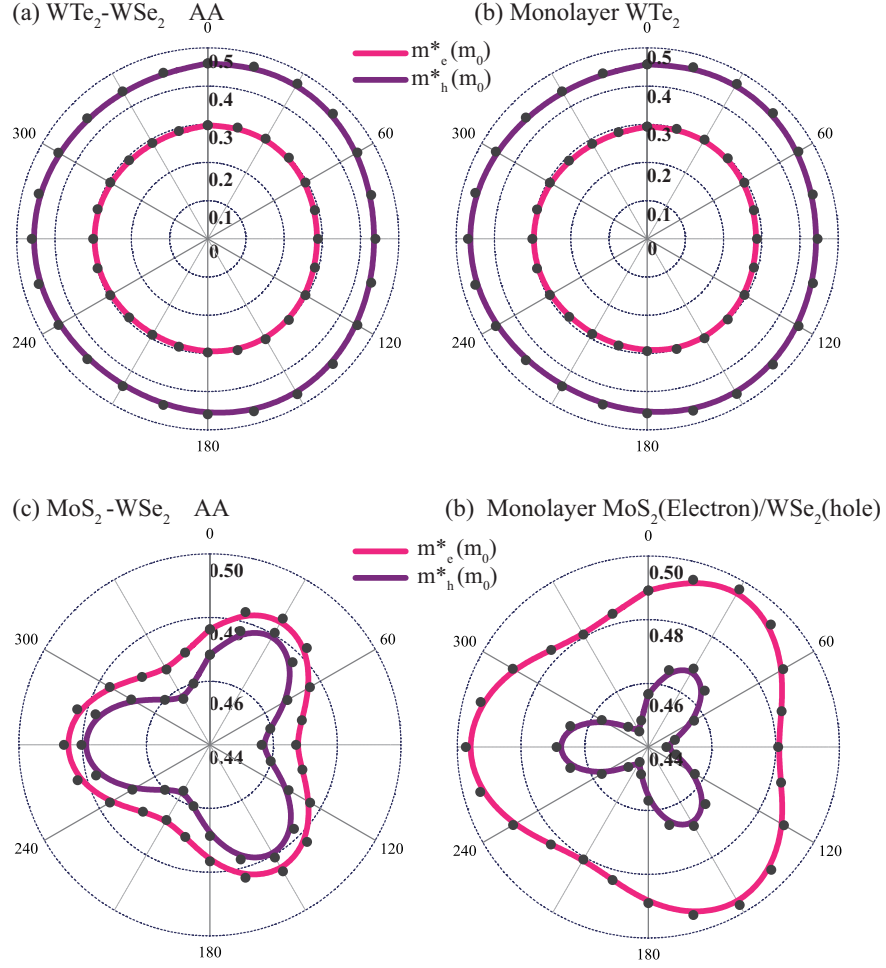


FIG. 5. The calculated carrier (hole mass $^*_h$  and electron mass $^*_e$ ) for (a) Type I band alignment system ( $\text{WTe}_2\text{-WSe}_2$  hetero-bilayer), (b) monolayer  $\text{WTe}_2$ , (c) Type II band alignment system ( $\text{MoS}_2\text{-WSe}_2$  hetero-bilayer), (d) monolayer  $\text{MoS}_2$  (electron) and  $\text{WSe}_2$  (hole)

monolayer  $\text{WSe}_2$  crystal, therefore, the  $m_e^*$  for  $\text{MoS}_2\text{-WSe}_2$  hetero-bilayer is similar to that of monolayer  $\text{MoS}_2$  and the  $m_h^*$  is similar to that of monolayer  $\text{WSe}_2$ , as shown in Fig. 5(c,d).

According to Eq. (1), the third factor determining carrier mobilities  $\mu$  is the deformation potential constants,  $D_l^{e,h}$ , which describes the scatterings of electrons/holes by longitudinal acoustic phonons. The calculated  $D_l^{e,h}$  for  $\text{MX}_2$  heterostructures and monolayer  $\text{MX}_2$  crystals are shown in TABLE II and TABLE S1, respectively. By comparison, it is found that, the deformation potential constants of  $\text{MX}_2$  heterostructures are overallly larger than those of constituent monolayer  $\text{MX}_2$ , which means that, the formation of the vdW  $\text{MX}_2$  heterostructures increases the electron-acoustic phonon coupling, leading to the increase of deformation potential constant  $D_l$ , especially for  $\text{MoS}_2\text{-WS}_2$  heterostructures.

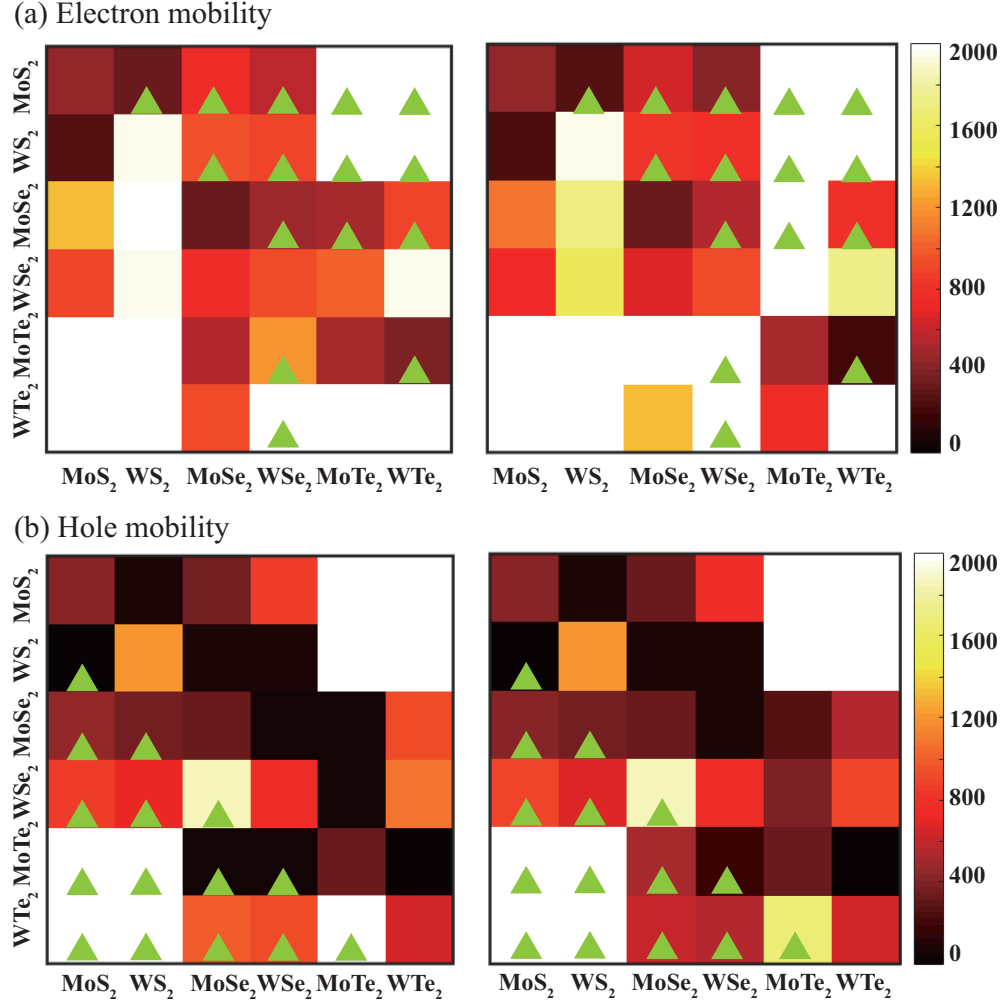


FIG. 6. The calculated carrier mobilities for the vdW  $\text{MX}_2$  heterostructures, with the AA stacking's in lower left corner and AB stacking's upper right corner respectively. The values along diagonal are the mobilities for monolayer  $\text{MX}_2$ . (a)(b) are the electron mobilities of the vdW  $\text{MX}_2$  heterostructures along armchair and zigzag directions, respectively; (c)(d) are the hole mobilities of the vdW  $\text{MX}_2$  heterostructures along armchair and zigzag directions, respectively.

Since the CBM and VBM of the  $\text{MX}_2$  heterostructures can be attributed to the respective band-structures of the constituent monolayer  $\text{MX}_2$ , according to the Anderson's rule, the shift of VBM from  $K$  point to  $\Gamma/M$  point will result in dramatic change of the deformation potential constants and effective holes masses for  $\text{MX}_2$  heterostructures with indirect bandgaps, e.g.  $\text{MoSe}_2$ - $\text{WSe}_2$ .

In order to figure out the exact contributions from the three factors, i.e. effective masses  $m_{e,h}^*$ , deformation potential constants  $D_l^{e,h}$  and elastic modulus  $C$ , to the carrier mobilities  $\mu$ , compared to the constituent monolayer  $\text{MX}_2$  crystals, we plotted the values of the three factors for constituent



monolayer crystals and hetero-bilayer structures in Fig. S4. It is clear that the elastic modulus of hetro-bilayer structures is nearly twice of the constituent monolayer  $\text{MX}_2$  crystals, the deformation potential constants of hetro-bilayer structures are overally larger or close to the constituent monolayer  $\text{MX}_2$  crystals except  $\text{MoTe}_2\text{-WTe}_2$ , the effective masses of hetro-bilayer structures mostly determined by the constituent monolayer cystals, are thus close to those of constituent monolayer crystals, except some hetro-bilayer structures with VBM points shifted from K to  $\Gamma/M$ , e.g.  $\text{MoTe}_2\text{-WTe}_2$ . Finally, the carrier mobility of electrons and holes along armchair and zigzag directions for the  $\text{MX}_2$  hetero-bilayer can be calculated according to Eq. (1), as shown in Fig. 6. The electron mobilities of hetro-bilayer structures are overally larger than those of constituent monolayer  $\text{MX}_2$  crystals, and the same situation takes place for the holes mobilities of hetro-bilayer structures with VBM located at K point. However, the holes mobilities of hetro-bilayer structures with VBM located at  $\Gamma/M$  point are smaller than those of constituent monolayer  $\text{MX}_2$  crystals.

The AA stacked  $\text{MoTe}_2\text{-MoSe}_2$  heterostructure possesses the highest electron mobility along zigzag direction, i.e.  $3658 \text{ cm}^2/(\text{V}\cdot\text{s})$ , and the AA stacked  $\text{MoTe}_2\text{-WTe}_2$  heterostructure possesses the highest hole mobility along the armchair direction, i.e.  $3285 \text{ cm}^2/(\text{V}\cdot\text{s})$ .

#### D. Optical properties of hetero-bilayer $\text{MX}_2$

The optical properties of the vdW  $\text{MX}_2$  heterostructures are described by the complex dielectric function, *i.e.*  $\epsilon(\omega) = \epsilon_1(\omega) + i\epsilon_2(\omega)$ . The imaginary part of dielectric tensor  $\epsilon_2(\omega)$  is determined by a summation over empty band states as follows<sup>71</sup>,

$$\epsilon_2(\omega) = \frac{2\pi e^2}{\Omega \epsilon_0} \sum_{k,v,c} \delta(E_k^c - E_k^v - \hbar\omega) \left| \langle \Psi_k^c | \mathbf{u} \cdot \mathbf{r} | \Psi_k^v \rangle \right|^2, \quad (4)$$

where  $\Omega$  is the crystal volume,  $\epsilon_0$  is the vacuum dielectric constant,  $\hbar\omega$  represents the photon energy,  $v$  and  $c$  mean the valence and conduction bands respectively,  $\mathbf{u}$  is the polarization vector in the incident electric field,  $\mathbf{u} \cdot \mathbf{r}$  is the momentum operator,  $\Psi_k$  is the wave function at the  $k$  point. The real part of dielectric tensor  $\epsilon_1(\omega)$  is obtained by the well-known Kramers-Kronig relation<sup>72</sup>,

$$\epsilon_1(\omega) = 1 + \frac{2}{\pi} P \int_0^\infty \frac{\epsilon_2(\omega') \omega'}{\omega'^2 - \omega^2 + i\eta} d\omega', \quad (5)$$

where  $P$  denotes the principle value. Based on the complex dielectric function, the absorption coefficient  $\alpha(\omega)$  is given by<sup>73,74</sup>

$$\alpha(\omega) = \frac{\sqrt{2}\omega}{c} \left\{ [\epsilon_1^2(\omega) + \epsilon_2^2(\omega)]^{1/2} - \epsilon_1(\omega) \right\}^{\frac{1}{2}}, \quad (6)$$

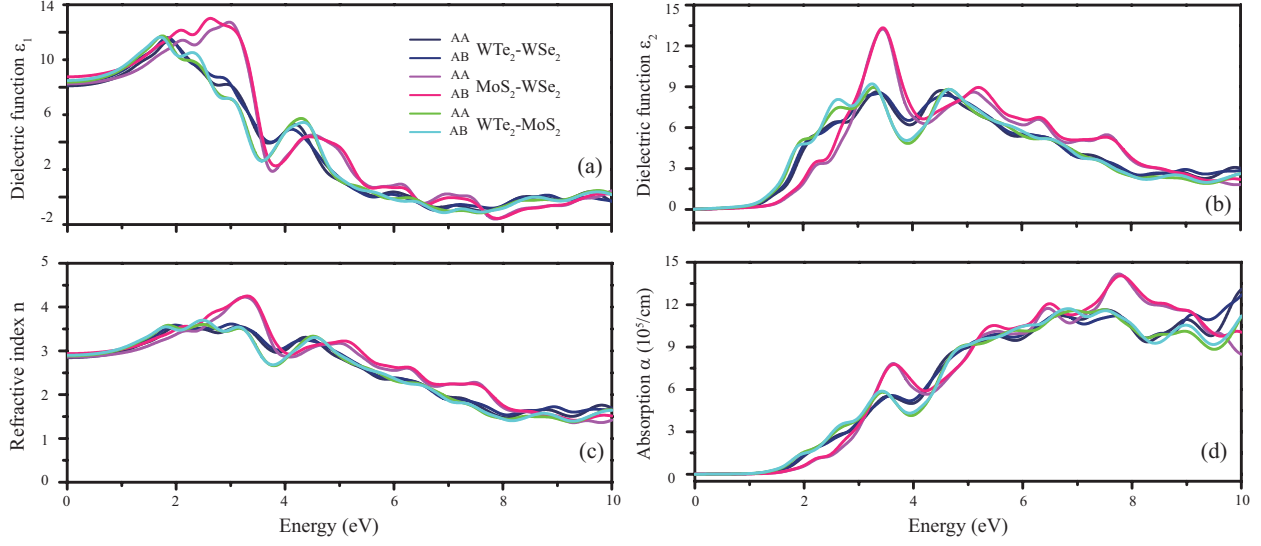


FIG. 7. HSE06 calculations of (a) the real part of the dielectric function, (b) the imaginary part of the dielectric function, (c) refractive and (d) optical absorption spectra of AA and AB stacking hetero-bilayer  $\text{WTe}_2\text{-WSe}_2$ ,  $\text{MoS}_2\text{-WSe}_2$  and  $\text{WTe}_2\text{-MoS}_2$  for incident light with the polarization along the  $a$ .

In 2D semiconductor materials, the band gap obtained by HSE06 is usually close to the real optical band gap due to the underestimation of band gap by neglecting excitonic effects<sup>75</sup>. Thus, we only performed HSE06 calculations to obtain optical properties for the hetero-bilayer  $\text{MX}_2$  under considerations here, which show that all of them are semiconductors with a finite band gap, as shown in TABLE I. All the optical constants are calculated for incident radiations with the electric field vector  $\mathbf{E}$  polarized along the  $a$  and  $b$  directions<sup>76</sup> shown in Fig. 1(c).

Due to the  $C_3$  symmetry of hexagonal structure of the hetero-bilayer  $\text{MX}_2$ , the dielectric function  $\epsilon(\omega)$  possesses the same results along the  $a$  and  $b$  directions. And the  $\epsilon(\omega)$  results for AA and AB stacking type are also close to each other, as shown in Fig. 7(a,b) and Fig. S4, irrespective of the corresponding Anderson band type. The similarity in  $\epsilon(\omega)$  results between AA and AB stacking hetero-bilayer  $\text{MX}_2$  can be understood by the fact that, the bandstructure of the hetero-bilayer  $\text{MX}_2$  can be roughly decomposed into the respective bandstructures of the constituent monolayer  $\text{MX}_2$  according to the Anderson's rule, thus the contribution to the total optical response, i.e.  $\epsilon_2(\omega)$ , from absorption of an incident photon  $\hbar\omega$  and then transition from  $\Psi_k^c$  to  $\Psi_k^v$  can be traced back to the behaviors of electrons located within the constituent monolayer  $\text{MX}_2$ . Therefore, the  $\epsilon_2(\omega)$  results for AA and AB stacking hetero-bilayer  $\text{MX}_2$  probably are similar since they contain identical constituent monolayer  $\text{MX}_2$ , according to Eq. 4.

The optical properties of hetero-bilayer  $\text{MX}_2$ , e.g.  $\text{WTe}_2\text{-WSe}_2$ ,  $\text{MoS}_2\text{-WSe}_2$  and  $\text{WTe}_2\text{-MoS}_2$ , are shown in Fig. 7. The main absorption peaks of these three hetero-bilayer  $\text{MX}_2$  locate in the range of 3.0 to 5.0 eV, i.e. the ultraviolet region, with a refractive range from 2.80 to 4.27 in this region.

#### IV. CONCLUSION

In this work, we have investigated the structure, electronic, mechanical, transport and optical properties of the vdW  $\text{MX}_2$  heterostructures using first-principles calculations. The AA and AB stacked hetero-bilayer  $\text{MX}_2$  exhibit three types of band alignment according to Anderson's rule, with a wide band gap range between 0 and 2 eV. The main differences between AA and AB stacked hetero-bilayer  $\text{MX}_2$  lie in the band structure and mechanical properties due to the inter-layer coupling such as the indirect  $\Gamma - K$  bandgap. The band structure of the  $\text{MTe}_2\text{-MX}_2$  will possess a higher valance band at  $M$  point due to the high band energy of  $5p_{x,y}$  orbitals of Te. The type II band alignment of the vdW hetero-bilayer  $\text{MX}_2$  make interlayer transitions possible, leading to spatially separated excitons. The transport properties of the vdW  $\text{MX}_2$  heterostructures are consistent with the symmetry of the geometric structures. It should be noted that the carrier mobilities of the hetero-bilayer  $\text{MX}_2$  are often higher than those of monolayer  $\text{MX}_2$ , attributed to the higher elastic modulus for the hetero-bilayer  $\text{MX}_2$ , while the hetero-bilayer  $\text{MX}_2$  with indirect bandgap possess much lower hole mobilities due to the increased effective masses and deformation potential constants. Furthermore, the calculated optical properties show strong optical absorption for vdW  $\text{MX}_2$  heterostructures, enabling the novel applications in optoelectronics from visible to ultraviolet region, such as photodetectors, light-emitting diodes, and photovoltaics.

#### ACKNOWLEDGEMENT

This work is supported by the National Natural Science Foundation of China under Grants No. 11374063 and 11404348, and the National Basic Research Program of China (973 Program) under Grant No. 2013CBA01505. Work at Ames Laboratory is partially supported by the U.S. Department of Energy, Office of Basic Energy Science, Division of Materials Science and Engineering (Ames Laboratory is operated for the U.S. Department of Energy by Iowa State University under Contract No. DE-AC02-07CH11358). The European Research Council under ERC

Advanced Grant No. 320081 (PHOTOMETA) supports work at FORTH.

## REFERENCE

---

\* <sup>†</sup>zhangh@fudan.edu.cn; <sup>‡</sup>hzshao@nimte.ac.cn; <sup>¶</sup>hyzhu@fudan.edu.cn

- <sup>1</sup> K. S. Novoselov, A. K. Geim, S. V. Morozov, D. Jiang, Katsnelson M. I., I. V. Grigorieva, and A. A. Dubonos, S. V. and Firsov. Two-dimensional gas of massless dirac fermions in graphene. *Nature*, 438:197–200, 2005.
- <sup>2</sup> Horst L. Stormer Yuanbo Zhang, Yan-Wen Tan and Philip Kim. Experimental observation of the quantum hall effect and berry’s phase in graphene. *Nature*, 438, 2005.
- <sup>3</sup> C. R. Dean, A. F. Young, I. Meric, C. Lee, L. Wang, S. Sorgenfrei, K. Watanabe, T. Taniguchi, P. Kim, K. L. Shepard, and J. Hone. Boron nitride substrates for high-quality graphene electronics. *Nature Nanotechnology*, 5(10):722–726, aug 2010.
- <sup>4</sup> Matthew Yankowitz, Jiamin Xue, Daniel Cormode, Javier D. Sanchez-Yamagishi, K. Watanabe, T. Taniguchi, Pablo Jarillo-Herrero, Philippe Jacquod, and Brian J. LeRoy. Emergence of superlattice dirac points in graphene on hexagonal boron nitride. *Nature Physics*, 8(5):382–386, mar 2012.
- <sup>5</sup> B. Radisavljevic, A. Radenovic, J. Brivio, V. Giacometti, and A. Kis. Single-layer mos2 transistors. *Nat. Nanotechnol.*, 6:147–150, 2011.
- <sup>6</sup> Andrea Splendiani, Liang Sun, Yuanbo Zhang, Tianshu Li, Jonghwan Kim, Chi-Yung Chim, Giulia Galli, and Feng Wang. Emerging photoluminescence in monolayer mos<sub>2</sub>. *Nano Lett.*, 10(4):1271–1275, 2010.
- <sup>7</sup> Du Xiang, Cheng Han, Jing Wu, Shu Zhong, Yiyang Liu, Jiadan Lin, Xue-Ao Zhang, Wen Ping Hu, Barbaros zyilmaz, A. H. Castro Neto, Andrew Thye Shen Wee, and Wei Chen. Surface transfer doping induced effective modulation on ambipolar characteristics of few-layer black phosphorus. *Nature Communications*, 6(1), mar 2015.
- <sup>8</sup> Likai Li, Yijun Yu, Guo Jun Ye, Qingqin Ge, Xuedong Ou, Hua Wu, Donglai Feng, Xian Hui Chen, and Yuanbo Zhang. Black phosphorus field-effect transistors. *Nat. Nanotechnol.*, 9(5):372–377, 2014.
- <sup>9</sup> Vy Tran, Ryan Soklaski, Yufeng Liang, and Li Yang. Layer-controlled band gap and anisotropic excitons in few-layer black phosphorus. *Physical Review B*, 89(23), jun 2014.

- <sup>10</sup> Marco Bernardi, Maurizia Palummo, and Jeffrey C. Grossman. Extraordinary sunlight absorption and one nanometer thick photovoltaics using two-dimensional monolayer materials. *Nano Letters*, 13(8):3664–3670, jul 2013.
- <sup>11</sup> D. Hennig and C. Mulhern. Collective transport of coupled particles. *The European Physical Journal B*, 85(1), jan 2012.
- <sup>12</sup> Wenxu Zhang, Zhishuo Huang, Wanli Zhang, and Yanrong Li. Two-dimensional semiconductors with possible high room temperature mobility. *Nano Research*, 7(12):1731–1737, sep 2014.
- <sup>13</sup> Ting Cao, Gang Wang, Wenpeng Han, Huiqi Ye, Chuanrui Zhu, Junren Shi, Qian Niu, Pingheng Tan, Enge Wang, Baoli Liu, and Ji Feng. Valley-selective circular dichroism of monolayer molybdenum disulphide. *Nature Communications*, 3(1), jan 2012.
- <sup>14</sup> Hualing Zeng, Junfeng Dai, Wang Yao, Di Xiao, and Xiaodong Cui. Valley polarization in mos2 monolayers by optical pumping. *Nat Nano*, 7(8):490–493, August 2012.
- <sup>15</sup> Filip A. Rasmussen and Kristian S. Thygesen. Computational 2d materials database: Electronic structure of transition-metal dichalcogenides and oxides. *The Journal of Physical Chemistry C*, 119(23):13169–13183, jun 2015.
- <sup>16</sup> Hiram J. Conley, Bin Wang, Jed I. Ziegler, Richard F. Haglund, Sokrates T. Pantelides, and Kirill I. Bolotin. Bandgap engineering of strained monolayer and bilayer MoS<sub>2</sub>. *Nano Letters*, 13(8):3626–3630, jul 2013.
- <sup>17</sup> Kin Fai Mak, Changgu Lee, James Hone, Jie Shan, and Tony F. Heinz. Atomically thin mos<sub>2</sub>: A new direct-gap semiconductor. *Phys. Rev. Lett.*, 105:136805, Sep 2010.
- <sup>18</sup> Thomas G. Pedersen, Christian Flindt, Jesper Pedersen, Niels Asger Mortensen, Antti-Pekka Jauho, and Kjeld Pedersen. Graphene antidot lattices: Designed defects and spin qubits. *Physical Review Letters*, 100(13), apr 2008.
- <sup>19</sup> Qihang Liu, Linze Li, Yafei Li, Zhengxiang Gao, Zhongfang Chen, and Jing Lu. Tuning electronic structure of bilayer MoS<sub>2</sub> by vertical electric field: A first-principles investigation. *The Journal of Physical Chemistry C*, 116(40):21556–21562, sep 2012.
- <sup>20</sup> K. S. Novoselov, A. Mishchenko, A. Carvalho, and A. H. Castro Neto. 2d materials and van der waals heterostructures. *Science*, 353(6298):aac9439, jul 2016.
- <sup>21</sup> S. J. Haigh, A. Gholinia, R. Jalil, S. Romani, L. Britnell, D. C. Elias, K. S. Novoselov, L. A. Ponomarenko, A. K. Geim, and R. Gorbachev. Cross-sectional imaging of individual layers and buried interfaces of graphene-based heterostructures and superlattices. *Nature Materials*, 11(9):764–767, jul

- 2012.
- <sup>22</sup> Wei-Ting Hsu, Zi-Ang Zhao, Lain-Jong Li, Chang-Hsiao Chen, Ming-Hui Chiu, Pi-Shan Chang, Yi-Chia Chou, and Wen-Hao Chang. Second harmonic generation from artificially stacked transition metal dichalcogenide twisted bilayers. *ACS Nano*, 8(3):2951–2958, feb 2014.
  - <sup>23</sup> Wenjing Zhang, Qixing Wang, Yu Chen, Zhuo Wang, and Andrew T S Wee. Van der waals stacked 2d layered materials for optoelectronics. *2D Materials*, 3(2):022001, apr 2016.
  - <sup>24</sup> Humberto Terrones, Florentino López-Urías, and Mauricio Terrones. Novel hetero-layered materials with tunable direct band gaps by sandwiching different metal disulfides and diselenides. *Scientific Reports*, 3(1), mar 2013.
  - <sup>25</sup> Pasqual Rivera, John R. Schaibley, Aaron M. Jones, Jason S. Ross, Sanfeng Wu, Grant Aivazian, Philip Klement, Kyle Seyler, Genevieve Clark, Nirmal J. Ghimire, Jiaqiang Yan, D. G. Mandrus, Wang Yao, and Xiaodong Xu. Observation of long-lived interlayer excitons in monolayer MoSe<sub>2</sub>–WSe<sub>2</sub> heterostructures. *Nature Communications*, 6:6242, feb 2015.
  - <sup>26</sup> Ming-Hui Chiu, Chendong Zhang, Hung-Wei Shiu, Chih-Piao Chuu, Chang-Hsiao Chen, Chih-Yuan S. Chang, Chia-Hao Chen, Mei-Yin Chou, Chih-Kang Shih, and Lain-Jong Li. Determination of band alignment in the single-layer MoS<sub>2</sub>/WSe<sub>2</sub> heterojunction. *Nature Communications*, 6:7666, jul 2015.
  - <sup>27</sup> H. Fang, C. Battaglia, C. Carraro, S. Nemsak, B. Ozdol, J. S. Kang, H. A. Bechtel, S. B. Desai, F. Kronast, A. A. Unal, G. Conti, C. Conlon, G. K. Palsson, M. C. Martin, A. M. Minor, C. S. Fadley, E. Yablonovitch, R. Maboudian, and A. Javey. Strong interlayer coupling in van der waals heterostructures built from single-layer chalcogenides. *Proceedings of the National Academy of Sciences*, 111(17):6198–6202, apr 2014.
  - <sup>28</sup> Xiaoping Hong, Jonghwan Kim, Su-Fei Shi, Yu Zhang, Chenhao Jin, Yinghui Sun, Sefaattin Tongay, Junqiao Wu, Yanfeng Zhang, and Feng Wang. Ultrafast charge transfer in atomically thin MoS<sub>2</sub>/WS<sub>2</sub> heterostructures. *Nature Nanotechnology*, 9(9):682–686, aug 2014.
  - <sup>29</sup> Hoseok Heo, Ji Ho Sung, Soonyoung Cha, Bo-Gyu Jang, Joo-Youn Kim, Gangtae Jin, Donghun Lee, Ji-Hoon Ahn, Myoung-Jae Lee, Ji Hoon Shim, Hyunyong Choi, and Moon-Ho Jo. Interlayer orientation-dependent light absorption and emission in monolayer semiconductor stacks. *Nature Communications*, 6(1), jun 2015.
  - <sup>30</sup> G. Kresse and J. Furthmüller. Efficient iterative schemes for *ab initio* total-energy calculations using a plane-wave basis set. *Phys. Rev. B*, 54:11169–11186, 1996.

- <sup>31</sup> John P. Perdew, Kieron Burke, and Matthias Ernzerhof. Generalized gradient approximation made simple. *Phys. Rev. Lett.*, 77:3865–3868, 1996.
- <sup>32</sup> Stefan Grimme. Semiempirical gga-type density functional constructed with a long-range dispersion correction. *Journal of Computational Chemistry*, 27(15):1787–1799, 2006.
- <sup>33</sup> Jochen Heyd, Gustavo E. Scuseria, and Matthias Ernzerhof. Hybrid functionals based on a screened coulomb potential. *J. Chem. Phys.*, 118(18):8207–8215, 2003.
- <sup>34</sup> J. Heyd, G. E. Scuseria, and M. Ernzerhof. Erratum: ybrid functionals based on a screened coulomb potential?[j. chem. phys. 118, 8207 (2003)]. *J. Chem. Phys.*, 124:219906, 2006.
- <sup>35</sup> Ling Tang, MengQiu Long, Dong Wang, and ZhiGang Shuai. The role of acoustic phonon scattering in charge transport in organic semiconductors: a first-principles deformation-potential study. *Sci. China Ser. B*, 52(10):1646–1652, 2009.
- <sup>36</sup> Y. Cai, G. Zhang, and Y.W Zhang. Polarity-reversed robust carrier mobility in monolayer mos<sub>2</sub> nanoribbons. *J. Am. Chem. Soc.*, 136:6269–6275, 2014.
- <sup>37</sup> Mengqiu Long, Ling Tang, Dong Wang, Yuliang Li, and Zhigang Shuai. Electronic structure and carrier mobility in graphdiyne sheet and nanoribbons: Theoretical predictions. *ACS Nano.*, 5(4):2593–2600, 2011.
- <sup>38</sup> J. Chen, J. Xi, D. Wang, and Z Shuai. Carrier mobility in graphyne should be even larger than that in graphene: A theoretical prediction. *J. Phys. Chem. Lett.*, 4:1443–1448, 2013.
- <sup>39</sup> Yanli Wang and Yi Ding. Electronic structure and carrier mobilities of arsenene and antimonene nanoribbons:a first-principle study. *Nanoscale Res. Lett.*, 10:254, 2015.
- <sup>40</sup> J. Bardeen and W. Shockley. Deformation potentials and mobilities in non-polar crystals. *Phys. Rev.*, 80:72–80, 1950.
- <sup>41</sup> W. Walukiewicz, H. E. Ruda, J. Lagowski, and H. C. Gatos. Electron mobility in modulation-doped heterostructures. *Physical Review B*, 30(8):4571–4582, oct 1984.
- <sup>42</sup> Shin ichi Takagi, Judy L. Hoyt, Jeffrey J. Welser, and James F. Gibbons. Comparative study of phonon-limited mobility of two-dimensional electrons in strained and unstrained si metal–oxide–semiconductor field-effect transistors. *Journal of Applied Physics*, 80(3):1567–1577, aug 1996.
- <sup>43</sup> J.A. Wilson and A.D. Yoffe. The transition metal dichalcogenides discussion and interpretation of the observed optical, electrical and structural properties. *Advances in Physics*, 18(73):193–335, may 1969.
- <sup>44</sup> Ganesh R. Bhimanapati, Zhong Lin, Vincent Meunier, Yeonwoong Jung, Judy Cha, Saptarshi Das, Di Xiao, Youngwoo Son, Michael S. Strano, Valentino R. Cooper, Liangbo Liang, Steven G. Louie,



- Emilie Ringe, Wu Zhou, Steve S. Kim, Rajesh R. Naik, Bobby G. Sumpter, Humberto Terrones, Fengnian Xia, Yeliang Wang, Jun Zhu, Deji Akinwande, Nasim Alem, Jon A. Schuller, Raymond E. Schaak, Mauricio Terrones, and Joshua A. Robinson. Recent Advances in Two-Dimensional Materials beyond Graphene. *ACS Nano*, 9(12):11509–11539, 2015.
- <sup>45</sup> Birman J L Burns G. *Introduction to Group Theory with Applications*. Academic Press, 1977.
- <sup>46</sup> J. H. Rose, John Ferrante, and John R. Smith. Universal binding energy curves for metals and bimetallic interfaces. *Physical Review Letters*, 47(9):675–678, aug 1981.
- <sup>47</sup> Jun Zhao, Yanle Li, and Jing Ma. Quantum spin hall insulators in functionalized arsenene (asx, x = f, oh and ch3) monolayers with pronounced light absorption. *Nanoscale*, 8:9657–9666, 2016.
- <sup>48</sup> W.J. Schutte, J.L. De Boer, and F. Jellinek. Crystal structures of tungsten disulfide and diselenide. *Journal of Solid State Chemistry*, 70(2):207–209, oct 1987.
- <sup>49</sup> R. Coehoorn, C. Haas, J. Dijkstra, C. J. F. Flipse, R. A. de Groot, and A. Wold. Electronic structure of mose<sub>2</sub>, mos<sub>2</sub>, and wse<sub>2</sub>. i. band-structure calculations and photoelectron spectroscopy. *Phys. Rev. B*, 35:6195–6202, Apr 1987.
- <sup>50</sup> K. D. Bronsema, J. L. De Boer, and F. Jellinek. On the structure of molybdenum diselenide and disulfide. *Zeitschrift f anorganische und allgemeine Chemie*, 540(9-10):15–17, sep 1986.
- <sup>51</sup> Ning Lu, Hongyan Guo, Lei Li, Jun Dai, Lu Wang, Wai-Ning Mei, Xiaojun Wu, and Xiao Cheng Zeng. MoS<sub>2</sub>/MX<sub>2</sub> heterobilayers: bandgap engineering via tensile strain or external electrical field. *Nanoscale*, 6(5):2879–2886, 2014.
- <sup>52</sup> Ziheng Ji, Hao Hong, Jin Zhang, Qi Zhang, Wei Huang, Ting Cao, Ruixi Qiao, Can Liu, Jing Liang, Chuanhong Jin, Liying Jiao, Kebin Shi, Sheng Meng, and Kaihui Liu. Robust stacking-independent ultrafast charge transfer in MoS<sub>2</sub>/WS<sub>2</sub> bilayers. *ACS Nano*, nov 2017.
- <sup>53</sup> Hong Jiang. Electronic band structures of molybdenum and tungsten dichalcogenides by the GW approach. *The Journal of Physical Chemistry C*, 116(14):7664–7671, mar 2012.
- <sup>54</sup> Jun Kang, Sefaattin Tongay, Jian Zhou, Jingbo Li, and Junqiao Wu. Band offsets and heterostructures of two-dimensional semiconductors. *Applied Physics Letters*, 102(1):012111, jan 2013.
- <sup>55</sup> Yi Ding, Yanli Wang, Jun Ni, Lin Shi, Siqi Shi, and Weihua Tang. First principles study of structural, vibrational and electronic properties of graphene-like MX<sub>2</sub> (m=mo, nb, w, ta;x=s, se, te) monolayers. *Physica B: Condensed Matter*, 406(11):2254–2260, may 2011.
- <sup>56</sup> K. Kośmider and J. Fernández-Rossier. Electronic properties of the MoS<sub>2</sub>-WS<sub>2</sub>heterojunction. *Physical Review B*, 87(7), feb 2013.



- <sup>57</sup> Wolfgang G. Zeier, Alex Zevalkink, Zachary M. Gibbs, Geoffroy Hautier, Mercouri G. Kanatzidis, and G. Jeffrey Snyder. Thinking like a chemist: Intuition in thermoelectric materials. *Angew. Chem. Int. Ed.*, 55(24):6826–6841, 2016.
- <sup>58</sup> R. L. Anderson. Germanium-gallium arsenide heterojunctions [letter to the editor]. *IBM Journal of Research and Development*, 4(3):283–287, jul 1960.
- <sup>59</sup> N Vol. What is what in the nanoworld: A handbook on nanoscience and nanotechnology. *Materials Today*, 7(12):49, dec 2004.
- <sup>60</sup> H. Fang, C. Battaglia, C. Carraro, S. Nemsak, B. Ozdol, J. S. Kang, H. A. Bechtel, S. B. Desai, F. Kronast, A. A. Unal, G. Conti, C. Conlon, G. K. Palsson, M. C. Martin, A. M. Minor, C. S. Fadley, E. Yablonovitch, R. Maboudian, and A. Javey. Strong interlayer coupling in van der waals heterostructures built from single-layer chalcogenides. *Proceedings of the National Academy of Sciences*, 111(17):6198–6202, apr 2014.
- <sup>61</sup> Shengli Zhang, Meiqiu Xie, Fengyu Li, Zhong Yan, Yafei Li, Erjun Kan, Wei Liu, Zhongfang Chen, and Haibo Zeng. Semiconducting group 15 monolayers: A broad range of band gaps and high carrier mobilities. *Angew. Chem. Int. Ed.*, 55(5):1666–1669, 2016.
- <sup>62</sup> Ming-Hui Chiu, Chendong Zhang, Hung-Wei Shiu, Chih-Piao Chuu, Chang-Hsiao Chen, Chih-Yuan S. Chang, Chia-Hao Chen, Mei-Yin Chou, Chih-Kang Shih, and Lain-Jong Li. Determination of band alignment in the single-layer MoS<sub>2</sub>/WSe<sub>2</sub> heterojunction. *Nature Communications*, 6:7666, jul 2015.
- <sup>63</sup> Bo Peng, Hao Zhang, Hezhu Shao, Ke Xu, Gang Ni, Jing Li, Heyuan Zhu, and Costas M. Soukoulis. Chemical intuition for high thermoelectric performance in monolayer black phosphorus, alpha-arsenene and aw-antimonene. *Journal of Materials Chemistry A*, 6(5):2018–2033, 2018.
- <sup>64</sup> Sverre Froyen and Walter A. Harrison. Elementary prediction of linear combination of atomic orbitals matrix elements. *Phys. Rev. B*, 20:2420–2422, Sep 1979.
- <sup>65</sup> Ning Lu, Hongyan Guo, Lei Li, Jun Dai, Lu Wang, Wai-Ning Mei, Xiaojun Wu, and Xiao Cheng Zeng. MoS<sub>2</sub>/MX<sub>2</sub> heterobilayers: bandgap engineering via tensile strain or external electrical field. *Nanoscale*, 6(5):2879–2886, 2014.
- <sup>66</sup> Félix Mouhat and François-Xavier Coudert. Necessary and sufficient elastic stability conditions in various crystal systems. *Physical Review B*, 90(22), dec 2014.
- <sup>67</sup> Bo Peng, Hao Zhang, Hezhu Shao, Zeyu Ning, Yuanfeng Xu, Gang Ni, Hongliang Lu, David Wei Zhang, and Heyuan Zhu. Stability and strength of atomically thin borophene from first principles calculations. *Materials Research Letters*, 5(6):399–407, November 2017.

- <sup>68</sup> R. C. Andrew, R. E. Mapasha, A. M. Ukpung, and N. Chetty. Mechanical properties of graphene and boronitrene. *Physical Review B*, 85(12), mar 2012.
- <sup>69</sup> Fan Zeng, Wei-Bing Zhang, and Bi-Yu Tang. Electronic structures and elastic properties of monolayer and bilayer transition metal dichalcogenides MX<sub>2</sub> (m = mo, w; x = o, s, se, te): A comparative first-principles study. *Chinese Physics B*, 24(9):097103, sep 2015.
- <sup>70</sup> Liping Yu, Qimin Yan, and Adrienn Ruzsinszky. Negative poisson's ratio in 1t-type crystalline two-dimensional transition metal dichalcogenides. *Nature Communications*, 8:15224, may 2017.
- <sup>71</sup> M. Gajdoš, K. Hummer, G. Kresse, J. Furthmüller, and F. Bechstedt. Linear optical properties in the projector-augmented wave methodology. *Phys. Rev. B*, 73:045112, 2006.
- <sup>72</sup> MS Dresselhaus. *Solid State Physics Part II Optical Properties of Solids*. Citeseer, 1999.
- <sup>73</sup> Sonali Saha, T. P. Sinha, and Abhijit Mookerjee. Electronic structure, chemical bonding, and optical properties of paraelectric batio<sub>3</sub>. *Phys. Rev. B*, 62:8828–8834, 2000.
- <sup>74</sup> Bingcheng Luo, Xiaohui Wang, Enke Tian, Guowu Li, and Longtu Li. Electronic structure, optical and dielectric properties of batio<sub>3</sub>/catio<sub>3</sub>/srtio<sub>3</sub> ferroelectric superlattices from first-principles calculations. *J. Mater. Chem. C*, 3:8625–8633, 2015.
- <sup>75</sup> Ji-Hui Yang, Yueyu Zhang, Wan-Jian Yin, XG Gong, Boris I Yakobson, and Su-Huai Wei. Two-dimensional sis layers with promising electronic and optoelectronic properties: theoretical prediction. *Nano letters*, 16(2):1110–1117, 2016.
- <sup>76</sup> Yuanfeng Xu, Hao Zhang, Hezhu Shao, Gang Ni, Jing Li, Hongliang Lu, Rongjun Zhang, Bo Peng, Yongyuan Zhu, Heyuan Zhu, and Costas M. Soukoulis. First-principles study on the electronic, optical, and transport properties of monolayer alpha - and beta -GeSe. *Physical Review B*, 96(24), dec 2017.